The Astrophysical Journal, 654:361–372, 2007 January 1

HIGH-RESOLUTION IMAGING OF MOLECULAR OUTFLOWS IN MASSIVE YOUNG STARS

Keping Qiu
Harvard-Smithsonian Center for Astrophysics, Cambridge, MA; and Department of Astronomy, Nanjing University, Nanjing, China; kqiu@cfa.harvard.edu

Qizhou Zhang
Harvard-Smithsonian Center for Astrophysics, Cambridge, MA

Henrik Beuther
Max-Planck-Institute for Astronomy, Heidelberg, Germany

and

Ji Yang
Purple Mountain Observatory, Chinese Academy of Sciences, Nanjing, China
Received 2006 June 30; accepted 2006 September 5

ABSTRACT

We present high angular resolution observations toward two massive star-forming regions, IRAS 18264−1152 and IRAS 23151+5912, with the Plateau de Bure Interferometer (PdBI) in the SiO($J = 2$–1) and $H^{13}CO^+$($J = 1$–0) lines and at 1.3 and 3.4 mm continuum, and with the Very Large Array (VLA) in the $NH_3(J, K) = (1, 1), (2, 2)$ lines. The NH_3(1, 1) and (2, 2) emission is detected toward IRAS 18264−1152 only. For IRAS 18264−1152, the SiO observations reveal at least two quasi-perpendicular outflows with high collimation factors, and the most dominant feature is a redshifted jetlike outflow with very high velocities up to about $\Delta v = 60$ km s^{-1} with respect to the systemic velocity. The very high velocity component ($\Delta v = 22$–60 km s^{-1}) of this outflow is spatially offset from its high-velocity ($\Delta v = 3$–21 km s^{-1}) component. The SiO line profiles and position-velocity characteristics of these two components suggest that this outflow could be driven by an underlying precessing jet. For IRAS 23151+5912, the bipolar but mainly blueshifted SiO outflow coincides with the inner parts of the single-dish CO outflow. In particular, the quasi-parabolic shape of the blueshifted outflow coincides with the near-infrared nebulosity and is consistent with entrainment of the gas by an underlying wide-angle wind. The analysis of the molecular outflow data of the two luminous sources further supports high-mass stars forming via a disk-mediated accretion process similar to that in low-mass stars.

Subject headings: ISM: individual (IRAS 18264−1152, IRAS 23151+5912) — ISM: jets and outflows — stars: formation

1. INTRODUCTION

The formation process of massive stars is poorly understood. There are two competing views: One view is that high-mass stars form via infall and disk-mediated accretion processes as a scaled-up version of their low-mass counterparts (e.g., Jijina & Adams 1996; Garay & Lizano 1999; Norberg & Maeder 2000; McKee & Tan 2002, 2003; Yorke & Sonnhalter 2002; Keto 2003). The other view argues that at the dense center of evolving massive clusters, competitive accretion could become a dominant process. In the extreme case, even the coalescence of low- and intermediate-mass (proto)stars may occur to form the most massive stellar objects (e.g., Bonnell et al. 1998, 2004; Stahler et al. 2000; Bally & Zinnecker 2005).

Massive molecular outflows play a very important role in massive star formation. In addition to dissipating excess angular momentum of the infalling material as in their low-mass counterparts (Shu et al. 1987), they may inject enough energy to sustain the turbulence and prevent a decrease of the virial parameter (Quillen et al. 2005), whose value may determine whether competitive accretion is effective in cluster-forming clouds (Krumholz et al. 2005a). Outflows also lead to significant anisotropy in the distribution of the circumstellar material, which greatly reduces the radiation pressure experienced by the infalling material (Krumholz et al. 2005b). The collimation factor of massive molecular outflows can help to discriminate between the disk-mediated accretion process and the coalescence process, since the former requires massive outflows as collimated as their low-mass counterparts and the latter predicts outflows to be far less collimated.

Surveys with single-dish telescopes find that massive molecular outflows are ubiquitous toward high-mass star-forming regions and are far more massive and energetic than their low-mass counterparts (e.g., Shepherd & Churchwell 1996; Zhang et al. 2001, 2005; Beuther et al. 2002c). While Shepherd & Churchwell (1996) find that massive outflows appear to be less collimated than their low-mass counterparts, Beuther et al. (2002c) argue that this may be mostly an observational artifact caused by the large distances of the target sources and the low spatial resolution of most studies. In recent years, there have been several high spatial resolution millimeter interferometric studies of molecular outflows toward massive star-forming regions. Shepherd & Kurtz (1999) reveal a massive outflow with a wide opening angle toward G192.16−3.82 and suggest that its driving mechanism is a strong wide-angle wind. Cesaroni et al. (1999) report a highly collimated SiO jet toward IRAS 20126+4104, and Shepherd et al. (2000) reveal the same but with a larger scale (2 pc) outflow in CO in a different orientation. Hunter et al. (1999) show a well-collimated SiO jet toward AFGL 5142. Beuther et al. (IRAS 05358+3543, 2002a; IRAS 19410+2336, 2003; IRAS 19217+1651, 2004) resolve simple outflows previously identified with single-dish observations into multiple and well-collimated outflows when

observed with interferometers at high spatial resolution. They find that their kinematics are similar to those of low-mass counterparts. Shepherd et al. (2003) present multiple, overlapping massive outflows driven by at least four protostars in the region of W75 N. Their energetics and near-infrared observations suggest that they are not likely to be scaled-up versions of jet-driven outflows from low-mass protostars. Gibb et al. (2003) show that a precessing jet-driven flow associated with G35.2−0.7N in single-dish observations can be explained as at least two overlapping flows. Su et al. (2004) reveal a clear bipolar morphology of molecular outflows toward two luminous sources, IRAS 21519+5613 and IRAS 22506+5944. Kumar et al. (2004) unveil at least four outflows toward an ultracompact (UC) H II region, Onsala 1. Finally, Sollins et al. (2004) resolve a highly energetic bipolar SiO outflow toward the UC H II region G5.89−0.39. All of these interferometric observations reveal new morphologies of massive outflows that cannot be resolved with single-dish observations and give a wealth of information about the physical process in the innermost parts of the massive star-forming regions.

Because the statistics of the high spatial resolution interferometric observations are still poor and some basic issues, such as collimation factors and the outflow driving mechanism, are being debated, we carry out a study of massive molecular outflows with the Plateau de Bure Interferometer (PdBI) and the Very Large Array (VLA). Here we use the shock tracer SiO(J = 2–1) to image outflows toward two massive star-forming regions, IRAS 18264−1152 and IRAS 23151+5912 (hereafter I18264 and I23151, respectively). The dense cores and ambient gas are mapped at 1.3 and 3.4 mm continuum and in the NH_3(1, 1) and (2, 2) and $H^{13}CO^+$(J = 1–0) lines. The two sources are part of a larger sample discussed in detail by Sridharan et al. (2002) and Beuther et al. (2002b, 2002d). Beuther et al. (2002c) present bipolar CO outflows toward the two sources with the IRAM 30 m telescope observations. Toward I23151, Weigelt et al. (2006) reveal a conelike nebulosity, which coincides with the blueshifted CO outflow, in the near-infrared K' band using the bispectrum speckle interferometry method. The kinematic distance of I23151, derived from the CS velocity, is 5.7 kpc. The kinematic distance of I18264 suffers from an ambiguity; it is either 3.5 or 12.5 kpc (Sridharan et al. 2002). S. Bontemps (2003, private communication) associated the region with larger scale sources with distances known via the near- and mid-infrared surveys 2MASS (Two Micron All Sky Survey) and *MSX* (*Midcourse Space Experiment*) and concluded that the region is at the near distance. On the other hand, Sewilo et al. (2004) determined the kinematic distance of an H II region, which is at a velocity of 50.9 km s^{-1} in the same direction as the line of sight of I18264, to be at 12.0 kpc. Sewilo et al. believe that the molecular cloud with a velocity of 43.6 km s^{-1} is associated with the H II region at 50.9 km s^{-1} and adopt a far distance of 12.4 kpc. Since the distance determinations above both use indirect methods and still give ambiguous results, we give physical parameter estimates corresponding to both the far and near distances in the following sections. Based on the High Resolution (HIRES) Infrared Astronomical Satellite (*IRAS*) database, Sridharan et al. (2002) estimate the luminosity of I23151 to be 10^5 $L_\odot$ and the luminosity of I18264 to be 10^4 $L_\odot$ and 1.2×10^5 $L_\odot$ for the near and far distances, respectively. As additional evidence of massive star formation and outflows, Class II CH_3OH and H_2O maser emission toward I18264 and H_2O maser emission toward I23151 is observed (Beuther et al. 2002d). Sridharan et al. (2002) detect no emission at 3.6 cm down to 1 mJy for both sources, while Zapata et al. (2006) detect 1.3 and 3.6 cm emission toward I18264 with a better sensitivity. After a description of observations in § 2, we show results in § 3. Discussion is presented in § 4, and we conclude in § 5.

2. OBSERVATIONS

The observations of I18264 and I23151 were carried out from 2003 August to November using the PdBI.[1] At the 3 mm wave band, the spectral correlator was set to sample the SiO(v = 0, J = 2–1) and $H^{13}CO^+$(J = 1–0) lines with a bandwidth of 40 MHz. In addition, two wide bands of 320 MHz were set to observe the continuum emission and to cover the SiO and $H^{13}CO^+$ lines as well. Taking advantage of the dual frequency operation, we set the correlator to the CN(J = 2–1) line using a bandwidth of 40 MHz and two 320 MHz wide bands at the 1 mm band for continuum. The CN(2–1) emission was not detected. Except for observations toward I23151 on 2003 December 9, all the tracks were carried out in weather conditions adequate for the 3 mm band only. I18264 was covered with a seven-field mosaic with pointing centers at (ΔR.A., Δdecl.) = (5″, 3.5″; 28″, 3.5″; −18″, 3.5″; 16.5″, 23.5″; −6.5″, 23.5″; 16.5″, −16.5″; −6.5″, −16.5″) with respect to the reference center at R.A.(J2000.0) = $18^h29^m14.3^s$ and decl.(J2000.0) = −11°50′26″. I23151 was observed with a single field with the pointing center at R.A.(J2000.0) = $23^h17^m21.0^s$ and decl.(J2000.0) = 59°28′49.00″. We used MWC 349 as the primary flux calibrator and 3C 273 and 3C 345 as the bandpass calibrators. The time dependence gain was monitored by observing B1741−038, B1830−210, and B2200+420. The visibility data were calibrated and imaged using the standard procedure in the GILDAS package. The systemic velocities are 43.6 km s^{-1} for I18264 and −54.4 km s^{-1} for I23151. The nominal spectral resolution was about 0.4 km s^{-1} and averaged to about 1 km s^{-1} for SiO(2–1). The continuum rms in the 3 mm band was ∼0.7 mJy for I18264 and ∼0.2 mJy for I23151.

The observations of the NH_3(1, 1) and (2, 2) lines were carried out on 1997 December 13 for I23151 in the D configuration and on 2001 July 23 for I18264 in the C configuration of the VLA.[2] In both observations, we used correlator mode 4, which provided 3.13 MHz bandwidth for the left and right polarizations of the (1, 1) and (2, 2) lines, respectively. The spectral resolution of the observations was 48 kHz, or 0.6 km s^{-1} at the NH_3 line frequencies. The pointing center of the observations was R.A.(J2000.0) = $18^h29^m14.31^s$, decl.(J2000.0) = −11°50′25.6″ for I18264 and R.A.(J2000.0) = $23^h17^m21.10^s$, decl.(J2000.0) = 59°28′48.6″ for I23151. The on-source integration per source was about 1 hr. The visibility data were calibrated and imaged in the AIPS package. The left and right polarizations were averaged during imaging to reduce the noise level in the data. The synthesized beam size was about 4″ for the I23151 images and 2.8″ × 2.0″ for the I18264 images. The rms noise level is 7 mJy per 0.6 km s^{-1} channel.

3. RESULTS

For both sources, we detected strong emission in SiO(J = 2–1) and $H^{13}CO^+$(J = 1–0). I18264 has detectable ammonia emission at an rms of 7 mJy per 0.6 km s^{-1} channel, and I23151 was not detected in NH_3 at an rms of 8 mJy per 0.6 km s^{-1} channel.

[1] This work is based on observations carried out with the IRAM Plateau de Bure Interferometer. IRAM is supported by INSU/CNRS (France), MPG (Germany), and IGN (Spain).

[2] The National Radio Astronomy Observatory is operated by Associated Universities, Inc., under cooperative agreement with the National Science Foundation.

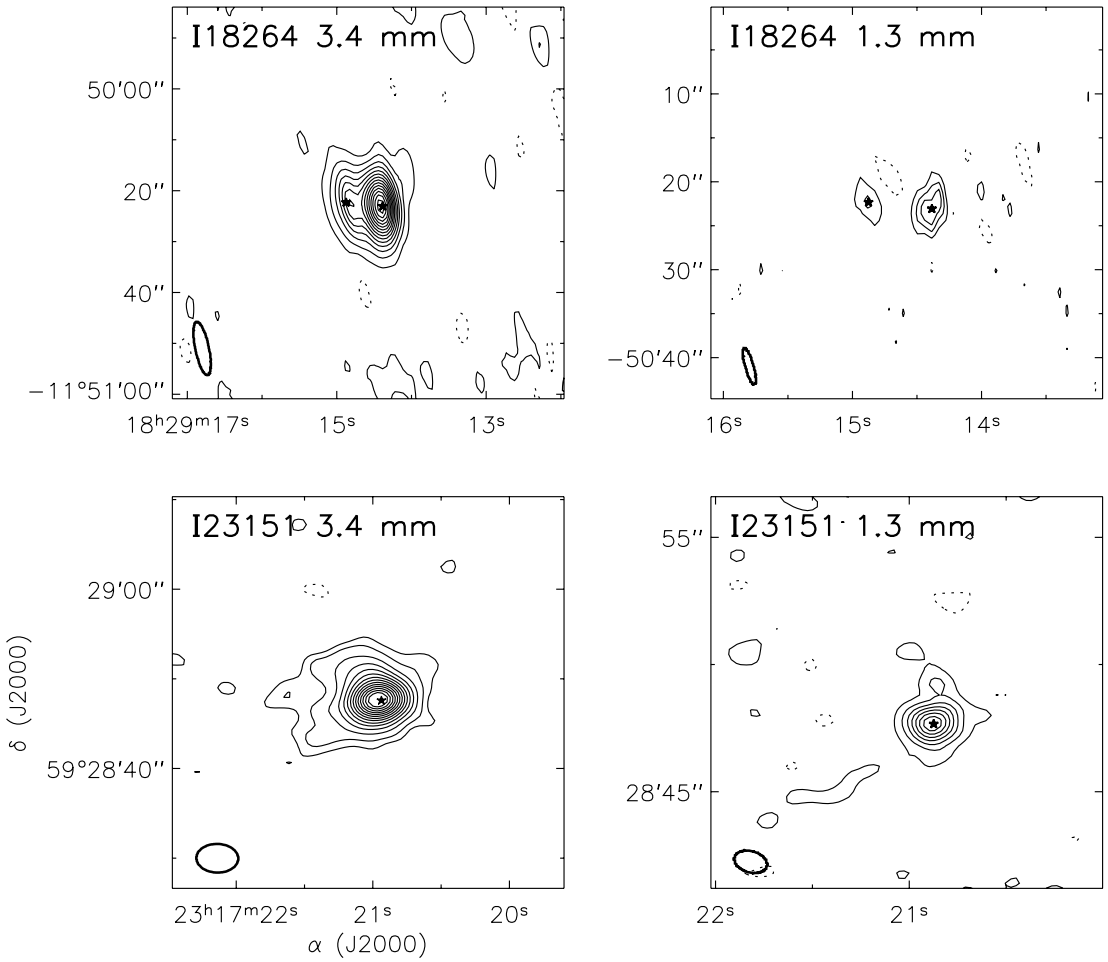

FIG. 1.—*Top*: The 3.4 mm (*left*) and 1.3 mm (*right*) continuum emission in I18264. The lowest contours and spacing are 2.1 mJy (3 σ) at 3.4 mm and 22.5 mJy (3 σ) at 1.3 mm. The dashed contours represent the -3 σ level. *Bottom*: Same as the top panel but for I23151. The lowest contours and spacing at 3.4 mm are 0.6 mJy (3 σ). At 1.3 mm, the contours start at 4.25 mJy (2.5 σ) in steps of 5.1 mJy (3 σ). The dashed contours represent the -3 σ level for 3.4 mm and -2.5 σ level for 1.3 mm. Here and below the stars mark the 1.3 mm continuum peaks. The beams are shown as thick ellipses at the bottom left of each panel.

3.1. *Millimeter Continuum Sources*

Figure 1 presents the 3.4 and 1.3 mm continuum emission of the two sources. For I18264, the 1.3 and 3.4 mm continuum emission resolves into two peaks with the stronger one in the west, while for I23151, the continuum emission remains singly peaked even at a resolution of $1.3'' \times 0.85''$ at 1.3 mm. For both sources, the peak positions at 1.3 and 3.4 mm coincide well with each other. In I23151, a fan-shaped structure opening to the east can be roughly identified in the 3.4 mm continuum emission. In the 1.3 mm continuum emission, there is a discontinuous arch structure at the lowest contour level that goes from a little bit northeast to the southeast of the millimeter continuum peak. We further discuss these features in § 3.2. Because the weather conditions were only adequate for the 3 mm wave band during the observing seasons, we use the 3.4 mm continuum data for quantitative analysis. Assuming that the 3.4 mm continuum is mainly produced by optically thin dust emission, we can calculate the masses of the dense cores following the relation $M_{\rm gas+dust} = F_\nu D^2/B_\nu(T_d)\kappa_\nu$ (Hildebrand 1983), where F_ν is the flux density of the dust emission, D is the distance to the source, and B_ν is the Planck function at a dust temperature of T_d. Sridharan et al. (2002) derive dust temperatures of 35 K for I18264 and 68 K for I23151 by graybody fits to the *IRAS* and millimeter

TABLE 1

DISTANCES AND DERIVED PHYSICAL PARAMETERS FOR THE TWO SOURCES

Source (1)	Distance (kpc) (2)	$M_{\rm core}$ ($M_\odot$) (3)	$M_{\rm dense}$ ($M_\odot$) (4)	$M_{\rm blue}$ ($M_\odot$) (5)	$M_{\rm red}$ ($M_\odot$) (6)	$M_{\rm out}$ ($M_\odot$) (7)	$\dot{M}_{\rm out}$ (10^{-4} $M_\odot$ yr^{-1}) (8)	$t_{\rm dyn}$ (10^4 yr) (9)
I18264	3.5	570	3900	3.2	17	20.2	34	0.5
	12.5	7300	50000	41	220	261	120	1.8
I23151	5.7	170	860	2.2	0.5	2.7	2.3	1.2

NOTES.—Col. (3): Mass of the dust-gas core derived from the 3.4 mm continuum emission. Col. (4): Mass of the dense ambient gas derived from the $H^{13}CO^+$ emission. Col. (5): Outflow mass derived from the blueshifted SiO emission. Col. (6): Outflow mass derived from the redshifted SiO emission. Col. (7): Total outflow mass derived from the sum of the blue- and redshifted outflow masses. Col. (8): Mass outflow rate derived from $M_{\rm red}$ for I18264 and from $M_{\rm out}$ for I23151. Col. (9): Dynamical timescale.

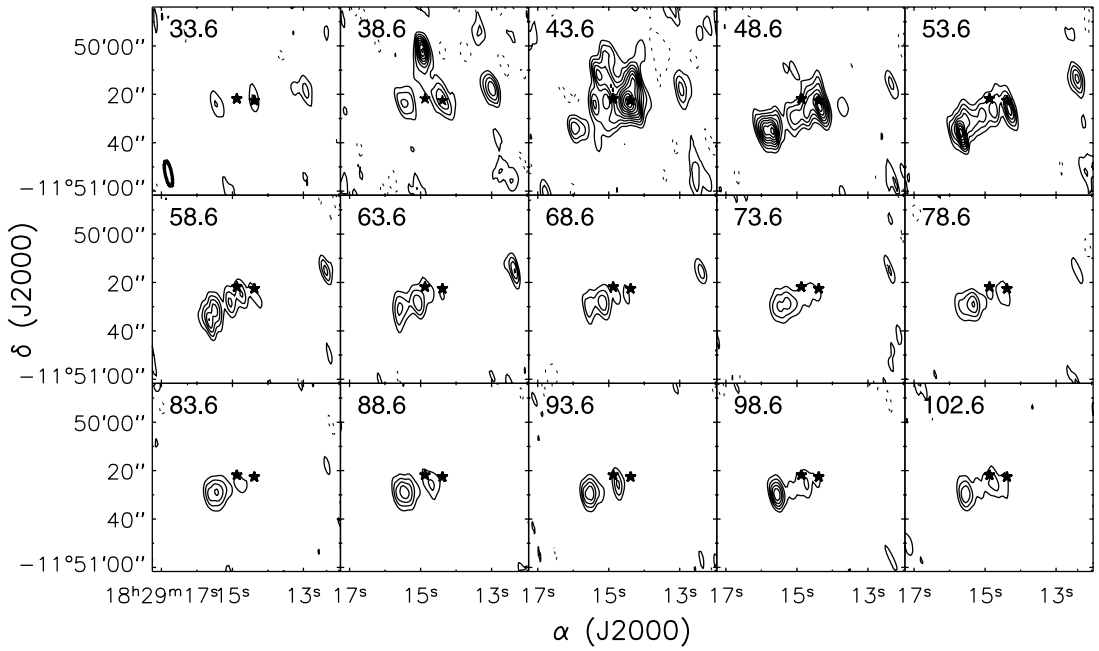

FIG. 2.—SiO channel maps in I18264, with a smoothed velocity resolution of 5 km s^{-1}. The contours start at 33 mJy (3 σ) in steps of 22 mJy (2 σ). The dashed contours represent the -3 σ level. The number in the top left of each panel denotes the central velocity of each channel. The thick ellipse in the bottom left of the first panel shows the beam size.

data. Here the dust opacity per gram is taken to be $\kappa_\nu = 0.1(\nu/1.2\ \mathrm{THz})^\beta\ \mathrm{cm}^2\ \mathrm{g}^{-1}$ (Hildebrand 1983), where the opacity index β is set to 1.5. The results of the calculations (M_{core}) are listed in Table 1. The uncertainty of this estimate mainly comes from the determinations of β and T_d. The masses will decrease by a factor of 4 if $\beta = 1$ and increase by a factor of 2 if T_d decreases to $T_d/2$. The integrated flux at 3.4 mm is 0.13 Jy for I18264 and 0.029 Jy for I23151. When compared with the 1.2 mm single-dish flux (Beuther et al. 2002a), the total flux from PdBI amounts to 63% for I18264 and 56% for I23151 of the single-dish flux extrapolated from 1.2 mm using $S(\nu) \propto \nu^{2+\beta}$ with $\beta = 1.5$. Some extended emission is not recovered by the interferometer.

3.2. SiO *Outflows*

Figure 2 presents the channel maps in SiO(2–1) in I18264, where the velocity resolution is smoothed to 5 km s^{-1}. The SiO emission mostly appears in the redshifted channels in Figure 2, and only the 38.6 km s^{-1} channel shows prominent blueshifted emission. The most remarkable feature in the channel maps is an elongated structure in the southeast. This redshifted emission has very high velocities up to $\Delta v \sim 60$ km s^{-1} with respect to the systemic velocity (v_{LSR}) 43.6 km s^{-1}. We have examined the data from the 320 MHz band and found that there is no detectable SiO emission beyond v_{LSR} of 110 km s^{-1}. The integrated blue- and redshifted SiO emission is shown in Figure 3*a*, where the single-dish bipolar CO outflow is resolved into two quasi-perpendicular outflows: The southeast to northwest (SE-NW) outflow and the northeast (NE) outflow. Both outflows seem to originate from the western peak of the millimeter continuum. Along the SE-NW outflow, both red- and blueshifted emission can be found, which is a typical feature for expanding bow shocks near the plane of the sky. From its alignment with the southeast jetlike outflow, the bipolar emission in the northwest seems to be the northwest lobe of the SE-NW outflow. But it is also possible that this feature is due to another low-mass (proto)star whose mass is below our detection limit. The two outflows are both well collimated with overall collimation factors ~3 for the NE outflow and ~4 for the SE-NW outflow. The estimated collimation factors should be the lower limits considering the unknown inclination angles and the spatial resolution limit. In Figure 3*b*, the redshifted SiO emission is shown in two velocity ranges, i.e., the high-velocity component (HC) with velocities $\Delta v = 3$–21 km s^{-1} and the very high velocity component (VHC) with velocities $\Delta v = 22$–60 km s^{-1}. The definitions of the velocity ranges here are based on the morphological changes in the SiO emission in the velocity channel maps and the characteristics in the position-velocity and mass-velocity diagrams that are discussed below. The redshifted southeast lobe (SE lobe) in the VHC is shifted toward north, and its remote peak is closer to the driving source

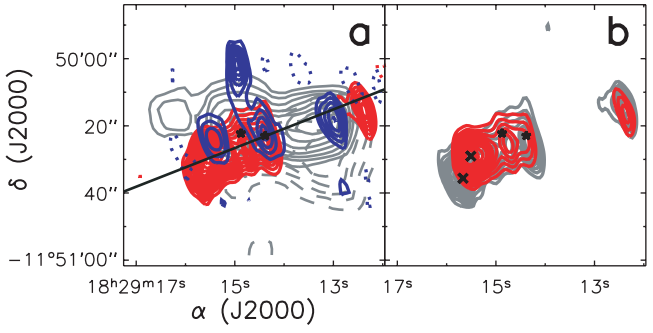

FIG. 3.—(*a*) Integrated SiO emission in I18264. The blue and red solid contours show the blue- and redshifted SiO emission, respectively. The blueshifted emission is integrated from 33.6 to 40.6 km s^{-1} with contour levels starting at 0.21 Jy km s^{-1} (3 σ) in steps of 0.14 Jy km s^{-1} (2 σ). The redshifted emission is integrated from 46.6 to 104.6 km s^{-1} with contour levels starting at 0.6 Jy km s^{-1} (3 σ) in steps of 0.4 Jy km s^{-1} (2 σ). The blue and red dashed contours represent the -3 σ level of the blue- and redshifted emission, respectively. The solid and dashed gray contours represent the blue- and redshifted lobes of the CO outflow in single-dish observations (Beuther et al. 2002c). The solid straight line denotes the axis along which the position-velocity (PV) diagram is plotted. (*b*) Same as (*a*), but here the gray and red contours denote the redshifted emission integrated from the HC channels and from the VHC channels, respectively. The gray contours start at 0.339 Jy km s^{-1} (3 σ) in steps of 0.226 Jy km s^{-1} (2 σ), and the red contours start at 0.486 Jy km s^{-1} (3 σ) in steps of 0.324 Jy km s^{-1} (2 σ). The two crosses mark the sites at which the SiO spectra are drawn.

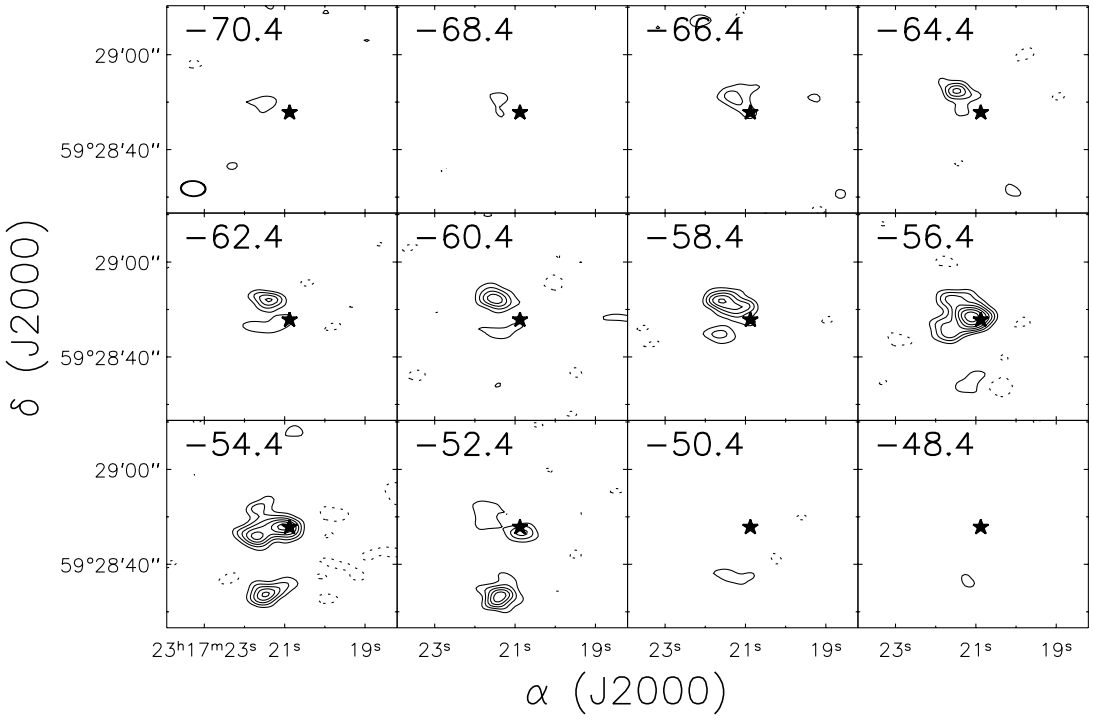

FIG. 4.—Same as Fig. 2, but for I23151 with 1 km s^{-1} resolution. The contours start at 16.5 mJy (3 σ) in steps of 11 mJy (2 σ).

than that in the HC. We discuss this jetlike outflow in detail in § 4.3. Using the continuous velocity structures in this dominant outflow, we derive the dynamical time following

$$t_{\rm dyn} = \frac{L_{\rm flow}}{\Delta v_{\rm max}},$$

where $L_{\rm flow}$ is the length of the jetlike SE lobe and $\Delta v_{\rm max}$ is the maximum velocity of the SE lobe. Assuming the optically thin thermal SiO(2–1) emission in local thermodynamic equilibrium (LTE), we estimate the gas mass in the outflow according to

$$N_{\rm SiO} = \frac{3k^2c^2}{2\pi^4 h\mu_d^2\nu^4}\frac{T_{\rm ex}}{\Delta\Omega}\exp\left(\frac{E_J + h\nu}{kT_{\rm ex}}\right)\int S_\nu\, dv,$$

$$M_{\rm out} = N_{\rm SiO}\left[\frac{\rm H_2}{\rm SiO}\right]\mu_g m_{\rm H_2} d^2\Delta\Omega,$$

where μ_d is the permanent dipole moment, $\Delta\Omega$ is the FWHM of the synthesized beam, $\mu_g = 1.36$ is the mean atomic weight of the gas, $m_{\rm H_2}$ is the mass of a hydrogen molecule, d is the distance of the source, S_ν is the flux density, and other symbols have common meanings. The mean excitation temperature $T_{\rm ex}$ is estimated to be 24 K from the $NH_3(1, 1)$, (2, 2) emission. It should be noted that $[H_2/SiO]$ has large uncertainty, since the SiO abundance can be greatly enhanced by shocks as a result of grain destruction leading to Si injection into the gas phase (Seab & Shull 1983). In contrast to the typical SiO abundance of 10^{-12} to 10^{-11} in dark clouds (Ziurys et al. 1989), Mikami et al. (1992) and Zhang et al. (1995) detect the SiO enhancement of 4–5 orders of magnitude toward the L1157 outflow. Hirano et al. (2001) estimate the SiO abundance to be 10^{-10} to 10^{-8} toward the multiple outflows in IRAS 16293−2422. We adopt an SiO abundance of 10^{-8}, which corresponds to an enhancement of 3–4 orders of magnitude with respect to that in dark clouds. Then the outflow

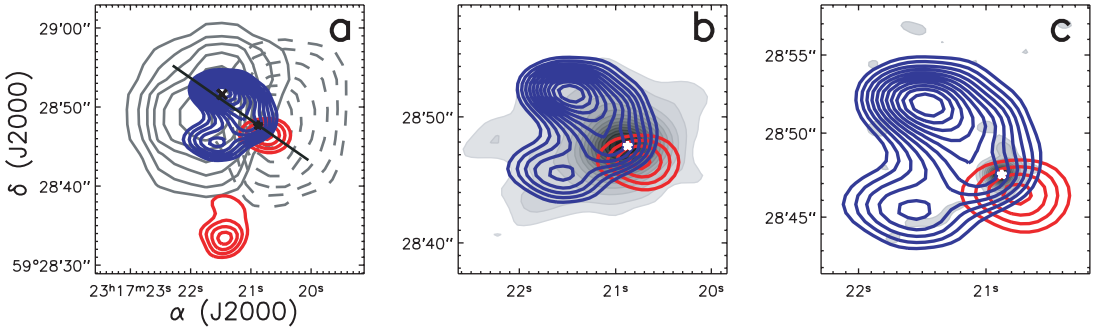

FIG. 5.—Iintegrated SiO emission in I23151. The blue and redshifted SiO emission in I23151, which are integrated from −68.4 to −55.4 km s^{-1} and from −53.4 to −50.4 km s^{-1}, respectively. The blue contours start at 0.115 Jy km s^{-1} (5 σ) in steps of 0.046 Jy km s^{-1} (2 σ), and the red contours start at 0.08 Jy km s^{-1} (5 σ) in steps of 0.032 Jy km s^{-1} (2 σ). The solid and dashed gray contours in (*a*) describe the blue- and redshifted CO outflow in single-dish observations (Beuther et al. 2002c). The solid straight line and the cross mark the axis for PV plotting and the site for the SiO spectrum drawing, respectively. The gray scale in (*b*) and (*c*) represent the 3.4 and 1.3 mm continuum emission, respectively.

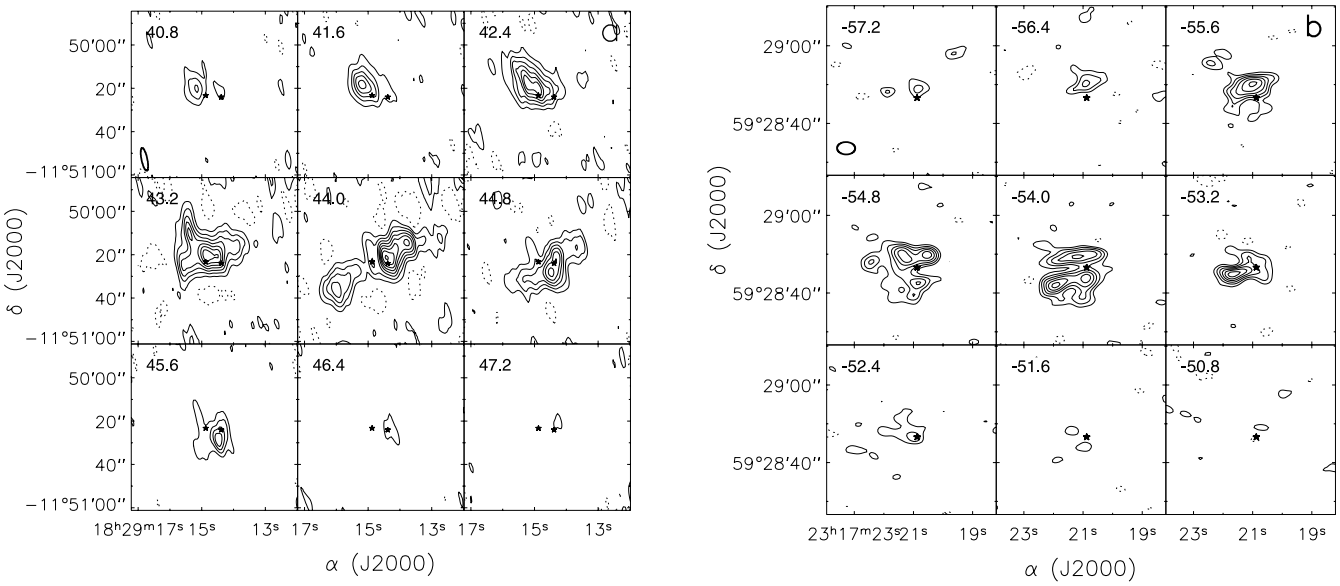

FIG. 6.—(*a*) $H^{13}CO^+$(1–0) channel maps for I18264. The lowest contours and spacing are 78 mJy (3 σ). The dashed contours represent the −3 σ level. The thick ellipse in the bottom left of the first panel shows the beam size. (*b*) Same as for (*a*), but for I23151. The contours start at 21 mJy (3 σ) in steps of 14 mJy (2 σ).

mass can be determined. Consequently, we get the outflow rate according to

$$\dot{M}_{\rm out} = \frac{M_{\rm out}}{t_{\rm dyn}}.$$

The derived results are listed in Table 1.

The channel maps with 1 km s^{-1} resolution in SiO in I23151 are presented in Figure 4. With respect to the systemic velocity −54.4 km s^{-1} ($v_{\rm LSR}$), the SiO emission is mainly blueshifted and extends to the velocity $\Delta v \sim -14$ km s^{-1}. The integrated emission is shown in Figure 5. In addition to the emission close to the millimeter continuum source, there is a weaker redshifted feature to the south. This may be an independent outflow from a low-mass (proto)star whose mass is below our detection limit. The bipolar SiO outflow seems to emanate from the millimeter continuum peak and coincides with the respective inner parts of the CO outflow from the single-dish observations (see Fig. 5*a*). The dominant blueshifted SiO outflow has a quasi-parabolic shape with the millimeter peak at its tip and a cavity in the center. This structure can also be identified in the channel maps, especially in the −56.4 km s^{-1} channel. Using the bispectrum speckle interferometry method, Weigelt et al. (2006) reveal a conelike nebulosity in the near-infrared K' band with a bright near-infrared point source at the tip. This nebulosity coincides well with the quasi-parabolic SiO outflow here. In Figures 5*b* and 5*c* the quasi-parabolic SiO outflow also coincides with the fan-shaped structure in the 3.4 mm continuum and the arch structure in the 1.3 mm continuum. The arch at 1.3 mm is detected only at the 2–3 σ level. However, the agreement with the 3.4 mm and the near-infrared image suggests that the structure is real. We also derive the characteristic parameters of the SiO outflow in I23151, where $T_{\rm ex}$ is assumed to be 30 K. The results are given in Table 1.

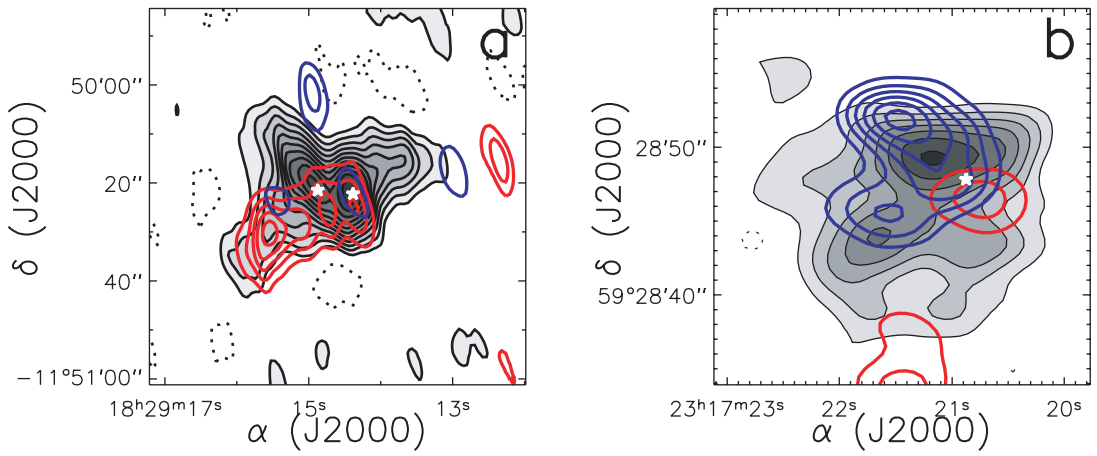

FIG. 7.—(*a*) Integrated $H^{13}CO^+$ emission. The gray scale and contours represent the $H^{13}CO^+$(1–0) emission integrated from 41.2 to 45.4 km s^{-1} for I18264, starting at 192 mJy km s^{-1} (4 σ) in steps of 144 mJy km s^{-1} (3 σ). The dashed contours represent the −4 σ level. The blue and red contours show the SiO outflow as in Fig. 3*a* but at the 5, 10, 15, 20, 25 σ levels. (*b*) Same as (*a*), but for I23151. The gray scale and contours represent the $H^{13}CO^+$(1–0) emission integrated from −56.0 to −52.8 km s^{-1}, starting at 36 mJy km s^{-1} (3 σ) in steps of 36 mJy km s^{-1}. The blue and red contours represent the integrated SiO emission as in Fig. 5 but at the 5, 9, 13, 17, 21, and 25 σ levels.

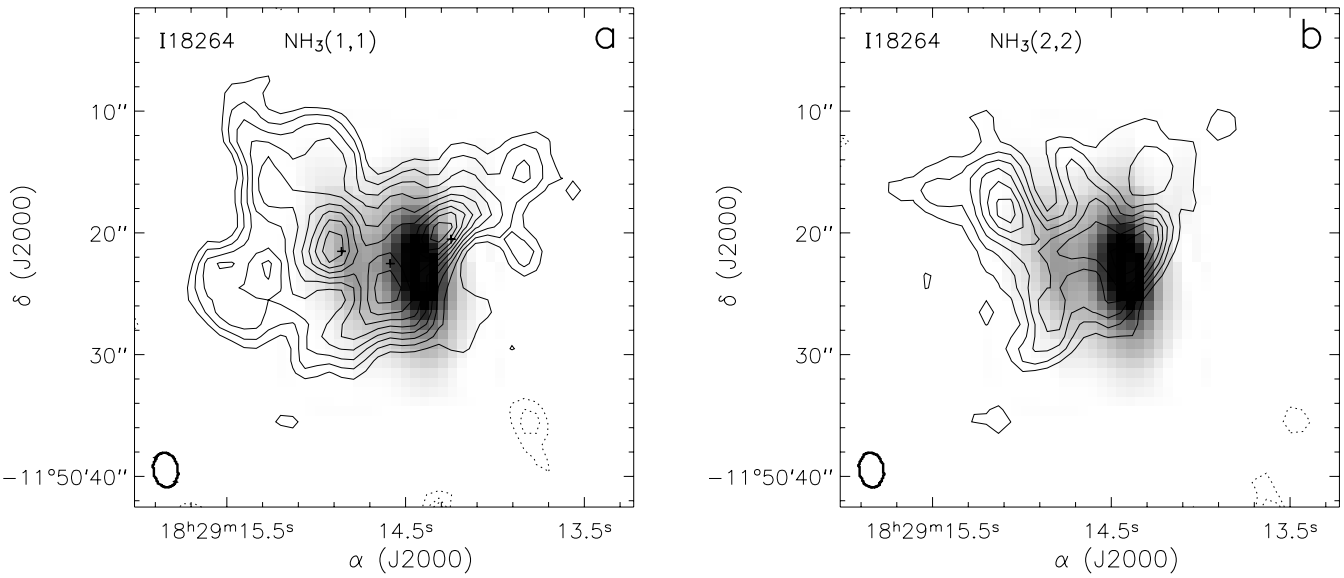

FIG. 8.—(*a*) $NH_3(1, 1)$ emission in I18264 integrated from 41.8 to 45.4 km s^{-1}. The contours start at 20 mJy km s^{-1} in steps of 13.4 mJy km s^{-1}. The plus signs denote the positions at which the physical parameters in Table 2 are calculated. (*b*) Same as (*a*), but for $NH_3(2, 2)$ emission integrated from 41.6 to 44.6 km s^{-1}. The contour levels start at 19.5 mJy km s^{-1} in steps of 13 mJy km s^{-1}. The dotted contours represent the -3 and -6 σ levels for both (*a*) and (*b*). The gray scale represents the 3.4 mm continuum. The beam sizes are marked at the bottom left of each panel.

3.3. $H^{13}CO^+$ *Condensations*

Figures 6*a* and 6*b* present the $H^{13}CO^+$ channel maps with 0.4 km s^{-1} resolution for I18264 and I23151, respectively. In both sources, the $H^{13}CO^+$ emission is limited to velocity channels around the systemic velocity, which confirms that this line emission mostly traces the dense ambient gas. For I18264, the peaks of the $H^{13}CO^+$ emission in the slightly blue- and redshifted channels approximately coincide with the western and eastern peaks of the millimeter continuum, respectively. Figures 7*a* and 7*b* present the integrated emission overlaid with the SiO outflows for the two sources. For I18264, the double peaks in the millimeter continuum are roughly resolved in the integrated $H^{13}CO^+$ emission. In addition to the condensations around the millimeter continuum peaks, the $H^{13}CO^+$ emission also shows extensions coincident with the SiO outflows. In particular, the southeast elongated feature in $H^{13}CO^+$ coincides well with the jetlike southeast SiO outflow. For I23151, the major and minor peaks in the integrated $H^{13}CO^+$ emission correlate well with the SiO clumps. The quasi-parabolic-shaped SiO outflow also has counterparts in $H^{13}CO^+$, especially in the -54.0 km s^{-1} channel and integrated emission. The correlation between the integrated $H^{13}CO^+$ emission and SiO emission for the two sources suggests that the $H^{13}CO^+$ gas may be influenced by the outflows. Adopting an HCO^+ abundance of 1×10^{-9} (van Dishoeck et al. 1993) and a C-to-^{13}C ratio of 67 (Langer & Penzias 1990), we can estimate the gas masses of the $H^{13}CO^+$ condensations with a method similar to that used in the estimation of the gas masses in the SiO outflows. The results ($M_{\rm dense}$) are listed in Table 1. Note that the masses derived from the $H^{13}CO^+$ emission are much larger than the core masses derived from the millimeter continuum. The integrated $H^{13}CO^+$ emission is much more extended than the interferometric millimeter continuum for both sources. Based on the single-dish 1.2 mm continuum observations, Beuther et al. (2002b) derive masses $\sim$2100 and $\sim$28,000 $M_\odot$, respectively, for the near and far distances for I18264 and $\sim$620 $M_\odot$ for I23151, which are consistent with the masses of the $H^{13}CO^+$ condensations here. Thus, the interferometric millimeter dust continuum probably traces the densest cores, filtering out most emission and hence yielding smaller masses, whereas the $H^{13}CO^+$ traces lower density gas and may even be slightly optically thick. In addition, the $H^{13}CO^+$ emission is obviously affected by the outflows, and HCO^+ and $H^{13}CO^+$ can be enhanced by shocks. Toward the bipolar molecular outflow of L1157, Bachiller & Gutiérrez (1997) detect the abundance of HCO^+ to be enhanced by a factor of 26–30. Jørgensen et al. (2004) reveal an HCO^+ abundance of 2.9×10^{-9} in the NGC 1333 outflow region. Girart et al. (2005) derive an averaged HCO^+ abundance of 3.2×10^{-9} over the core located ahead of HH2. Thus, the abundance of HCO^+ can be enhanced by a factor of $\sim$3–30. Assuming the $H^{13}CO^+$ to HCO^+

TABLE 2
PHYSICAL PARAMETERS DERIVED FROM THE AMMONIA EMISSION FOR I18264

Position[a]	$\tau(1, 1, m)$	$T_{\rm rot}(2, 2{:}1, 1)$ (K)	$T_{\rm ex}$ (K)	$T_{\rm kin}$ (K)	$n(H_2)$ (10^5 cm^{-3})	Δv (km s^{-1})
Left	4.0	24	23	30	1.6	3.1
Middle	2.7	30	25	45	1.0	1.9
Right	2.7	24	24	32	1.6	2.5
Mean[b]	3.1	26	24	36	1.4	2.5

[a] Marked as plus signs in Fig. 8*a*.
[b] Averaged from the three positions.

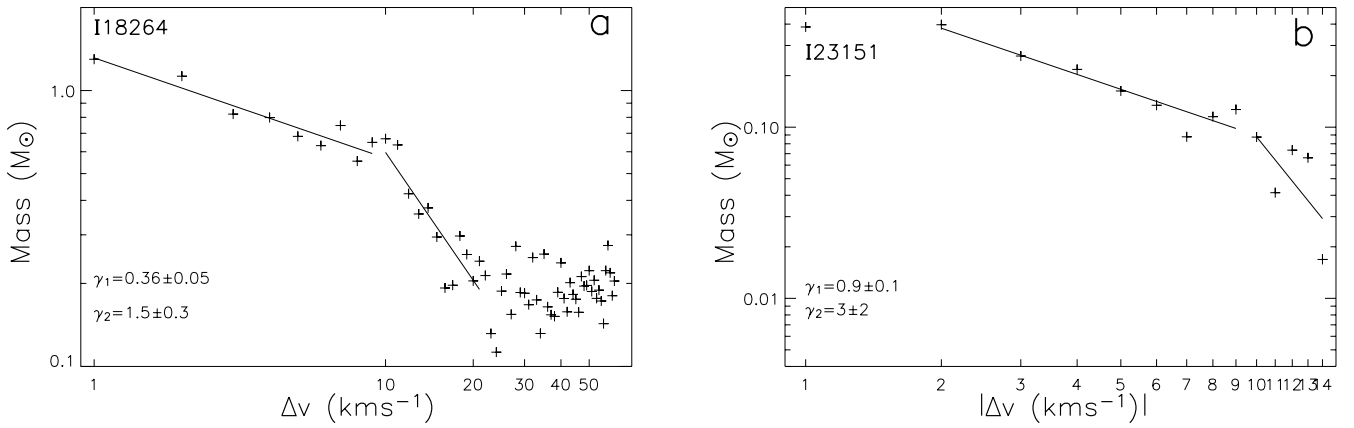

FIG. 9.—(*a*) Outflow masses calculated for the near distance for the 1 km s^{-1} channels as a function of flow velocities for I18264. Note that outflow masses for the far distance will give the same broken power law. (*b*) Same as (*a*), but for I23151. The solid lines show the power-law fits of $m(v) \propto v^{-\gamma}$.

ratio to be constant, the abundance of $H^{13}CO^+$ may be underestimated, and consequently the mass would be overestimated by a factor of ~3–30.

3.4. *Ammonia Emission*

Sridharan et al. (2002) detected the $NH_3(J, K) = (1, 1), (2, 2)$ inversion lines toward I18264 with the Effelsberg 100 m telescope. The NH_3 emission toward I23151 was also detected with the Effelsberg telescope, but it is about an order of magnitude weaker than for I18264 (H. Beuther 2006, private communication). With the VLA we observed the NH_3(1, 1) and (2, 2) lines toward the two regions and detected the NH_3(1, 1) and (2, 2) emission only in I18264. We derive the optical depth $\tau(1, 1, m)$ for the main component of the NH_3(1, 1) line and the rotational temperature $T_{\rm rot}$(2, 2:1, 1) (Ho & Townes 1983) at three positions as denoted in Figure 8*a*. The kinetic temperature $T_{\rm kin}$ can be estimated according to

$$T_{\rm rot}(2,2{:}1,1) = \frac{T_{\rm kin}}{1 + (T_{\rm kin}/41.7)\ln[1 + C(2,2 \rightarrow 2,1)/C(2,2 \rightarrow 1,1)]},$$

where $C(2,2 \rightarrow 2,1)$ and $C(2,2 \rightarrow 1,1)$ are the rates of collisional transition between the levels (2, 2), (2, 1), and (1, 1) (Walmsley & Ungerechts 1983; Danby et al. 1988). The excitation temperature $T_{\rm ex}$ is determined following

$$T_B(1,1,m) = (T_{\rm ex} - 2.7)\left(1 - e^{-\tau(1,1,m)}\right),$$

where $T_B(1, 1, m)$ is the brightness temperature of the main component of the NH_3(1, 1) line. Then the gas density $n(H_2)$ can be calculated according to

$$n(\mathrm{H_2}) = \frac{A}{C}\left(\frac{T_{\rm ex} - 2.7}{T_{\rm kin} - T_{\rm ex}}\right)\left(1 + \frac{kT_{\rm kin}}{h\nu}\right),$$

where A and C are the Einstein A coefficient and the collision rate, respectively (Ho & Townes 1983). The results derived from the ammonia emission are listed in Table 2. The derived mean rotation temperature 26 K is a little higher than that of 18 K derived by Sridharan et al. (2002), and the mean kinetic temperature 36 K is approximately equal to the dust temperature (Sridharan et al. 2002). In Figure 8, there are peaks in NH_3(1, 1) and (2, 2) that are approximately coincident with the millimeter continuum peaks. It seems that the NH_3(1, 1) and (2, 2) lines trace a more extended envelope than the millimeter continuum does. The derived gas density is $\sim(1.4 \pm 0.6) \times 10^5$ cm^{-3}, and the intrinsic line width (FWHM) is ~2.5 km s^{-1}.

4. DISCUSSION

4.1. *Outflow Energetics*

In I18264, the SiO emission reveals two quasi-perpendicular molecular outflows emanating from the western millimeter peak. The mass estimated from the millimeter continuum is as high as 570 and 7300 $M_\odot$ for the near and far distances, respectively, even with a fraction of the flux being filtered out by the interferometer. Since the western peak is much stronger than the eastern one, most of the mass is attributed to the western peak. To check the missing short spacings, the convolved PdBI SiO data have been compared with the single-dish SiO data observed with the IRAM 30 m telescope (H. Beuther 2006, private communication). We find that at channels around the systemic velocity 43.6 km s^{-1}, less than 34% of the SiO flux is filtered out by the interferometer, while at channels above $v_{\rm LSR}$ of 50 km s^{-1}, no missing short spacing problem occurs. The outflow mass for I18264 in Table 1 is derived from channels of 33.6–40.6 km s^{-1} ($M_{\rm blue}$) and 46.6–103.6 km s^{-1} ($M_{\rm red}$), which are both 3 km s^{-1} apart from the systemic velocity. So the derived outflow mass for I18264 does not suffer much from missing short spacings, and the results are comparable to that derived from the single-dish CO observations (Beuther et al. 2002c). From the SiO channel maps and the integrated emission $M_{\rm red}$ is mostly due to the jetlike SE lobe and gives mass outflow rates of 3.4×10^{-3} and 1.2×10^{-2} $M_\odot$ yr^{-1} for the near and far distances, respectively. With the assumption of momentum conservation between the observed outflow and the internal jet and adopting a typical jet velocity of 500 km s^{-1}, the mass-loss rates caused by the underlying jet or wind are about 4.1×10^{-4} and 1.4×10^{-3} $M_\odot$ yr^{-1} for the near and far distances, respectively. Furthermore, assuming a ratio between the mass-loss rate and the accretion rate of approximately $\frac{1}{3}$ (Shu et al. 1987; Tomisaka 1998), we get accretion rates of 1.2×10^{-3} and 4.2×10^{-2} $M_\odot$ yr^{-1} for the near and far distances, respectively. Such accretion rates are high enough to overcome the radiation pressure of the central (proto)star and form most massive stars (Wolfire & Cassinelli 1987; Jijina & Adams 1996; Yorke & Sonnhalter 2002). For I23151, the estimation from the millimeter continuum gives a core of 170 $M_\odot$. With the same assumptions as for I18264, the outflow rate 2.3×10^{-4} $M_\odot$ yr^{-1} will lead to an accretion rate of 1.9×10^{-5} $M_\odot$ yr^{-1}. According to the comparison between the convolved PdBI SiO data and those

from the IRAM 30 m single-dish observations (H. Beuther 2006, private communication), about 32%–43% of the flux is filtered out by the interferometer for most velocity channels. Because of the missing flux due to the missing short spacings and the outflow being mostly blueshifted, the accretion rate could be underestimated. Therefore, the accretion rate for I23151 could be high enough to overcome the radiation pressure and form massive stars (Wolfire & Cassinelli 1987; Jijina & Adams 1996; Yorke & Sonnhalter 2002).

4.2. *Mass-Velocity Diagrams*

Outflows associated with low-mass young stellar objects (YSOs) usually exhibit a "mass spectrum" $m_{\rm CO}(v) \propto v^{-\gamma}$ (e.g., Chandler et al. 1996; Lada & Fich 1996). The power-law index γ is typically $\sim$1.7–1.8 (Lada & Fich 1996), although the slope often steepens at velocities greater than 10 km s^{-1} from the systemic velocity. From a compilation of 22 sources with luminosities ranging from 0.58 to 3×10^5 $L_\odot$, Richer et al. (2000) find that at velocities below 10 km s^{-1}, γ is similar, while at velocities above 10 km s^{-1}, γ is 3–4 for low-mass YSOs and 3–8 for luminous YSOs. Toward a sample of 11 objects with luminosities $L_{\rm bol} \geq 10^2$ $L_\odot$ at a distance of 2 kpc, Ridge & Moore (2001) find neither a correlation between mass-spectrum slope and bolometric luminosity nor a clear separation between γ-values measured for the high-velocity and low-velocity emission. Su et al. (2004) also study the mass-velocity diagrams of outflows of two luminous YSOs and find a change in slope at a break-point velocity of 10 km s^{-1}. They suggest that the high-velocity ($|\Delta v| >$ 10 km s^{-1}) gas may drive the low-velocity ($|\Delta v| < 10$ km s^{-1}) gas. With the assumption of the optically thin SiO thermal emission in LTE, we derive the mass-velocity diagrams for the SiO outflows for the two sources (see Fig. 9). Since the SiO emission is predominantly redshifted in I18264 and blueshifted in I23151, we derive the mass-velocity relations in the corresponding wings for the two sources. The redshifted emission in I18264 is mostly attributed to the SE lobe. Thus, Figure 9*a* represents the mass-velocity relationship of the HC of the SE lobe and can be fitted by a broken power law with the index steepening from $\gamma_1 = 0.36 \pm 0.05$ to $\gamma_2 = 1.5 \pm 0.3$ at $\Delta v =$ 10 km s^{-1}. The mass distribution in the velocity channels of the VHC of the SE lobe has large scatter and can hardly be described by a linear fit. Similarly, the blueshifted lobe of the SiO outflow in I23151 is also fitted by a broken power law with $\gamma_1 = 0.9 \pm 0.1$ for $|\Delta v| < 10$ km s^{-1} and $\gamma_2 = 3 \pm 2$ for $|\Delta v| \geq 10$ km s^{-1}. From three-dimensional simulations of a dense molecular jet penetrating a dense molecular medium, Smith et al. (1997) predict the change in slope at high velocities due to a jet-bow shear layer consisting of molecules that survived the jet terminal shock. Models of material being accelerated by jet-driven bow shocks (Downes & Ray 1999) have reproduced a power-law relationship between mass and velocity with γ increasing with decreasing molecular abundance in the jet. However, Downes & Ray (1999) give an upper limit of 3.75 for γ, which is much less than the observed values. Therefore, the physical origin of the broken power law in the mass-velocity diagrams is still unclear.

4.3. *Kinematics*

The SiO in the gas phase of molecular outflows could be produced through the sputtering of Si-bearing material in grains, with the sputtering driven by neutral particle impact on charged grains in shocks (Schike et al. 1997). In Figure 7*a*, the jetlike SE lobe in I18264 coincides well with the H^{13}CO$^+$ structure extending to the southeast, suggesting the SiO emission in this region may arise from the interaction between the shocks driven

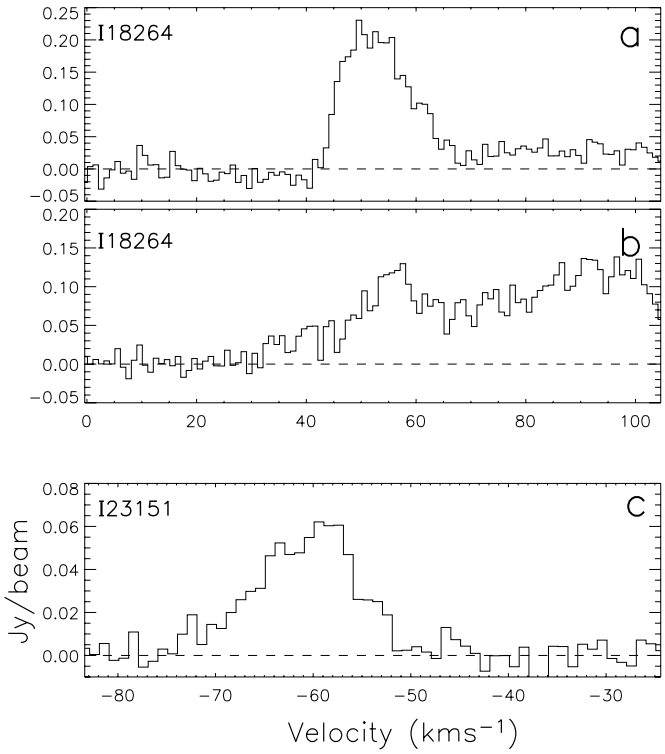

FIG. 10.—(*a*) SiO line profile of I18264 at the position denoted by the southern cross in Fig. 3*b*. (*b*) Same as (*a*), but at the position denoted by the northern cross in Fig. 3*b*. (*c*) SiO line profile of I23151 at the position denoted by the cross in Fig. 5*a*.

by the jet or wind from the central (proto)star and the dense ambient gas clump. Such an interaction mainly exists in the redshifted lobe, since the SiO emission is predominantly redshifted. In Figure 10*a*, the SiO line at the downstream peak of the HC of the SE lobe (Fig. 3*b*, *southern cross*) shows a profile with a steep decrease toward the systemic velocity and a gradual redshifted wing, which suggests that the SiO enhancement arises from the quiescent material accelerated by the shock when the jet or wind impinges on the dense ambient gas. We have checked the corresponding single-dish SiO spectrum and found that such a profile also exists. So the steep decrease toward the systemic velocity cannot be due to the missing short spacings. These kinds of SiO profiles and interactions have been observed toward several low-mass outflows (e.g., Zhang et al. 1995; Hirano et al. 2001). The line profile at the downstream peak of the VHC (Fig. 3*b*, *northern cross*) shows a very broad plateau in the redshifted wing with velocities up to about 60 km s^{-1} from the systemic velocity (see Fig. 10*b*). Such a broad plateau is consistent with the flattened mass spectrum of the VHC in the mass-velocity diagram. For I23151, there is a good correlation between the SiO clumps and the integrated H^{13}CO$^+$ peaks. The SiO line at the peak of the blueshifted lobe (Fig. 5, *cross*) also shows a profile of a steep drop toward the systemic velocity and a gradual decline in the blueshifted wing (see Fig. 10*c*), and this profile is confirmed in the single-dish data. Thus, the SiO emission in I23151 could also arise from the interaction between the jet or wind driven by the central (proto)star and the dense ambient gas.

Toward several low-luminosity sources (e.g., L1448, Guilloteau et al. 1992; NGC 2264G, Lada & Fich 1996), it is observed that the flow velocity increases with distance from the driving source. On the contrary, Zhang et al. (2000) find that the SiO outflow velocities in L1157 decrease toward the clumps farther away from the driving source. They also consider the different orientations

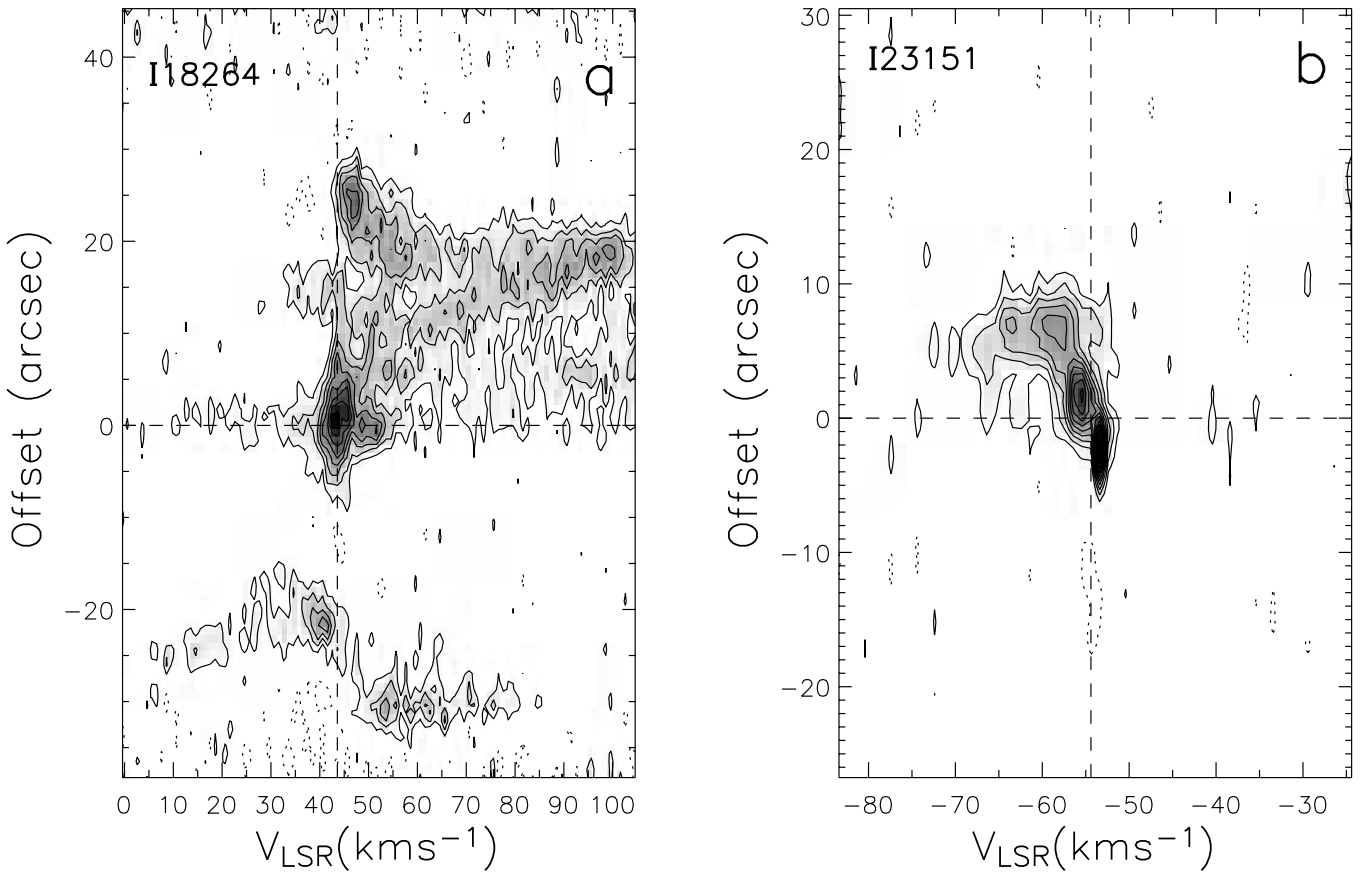

FIG. 11.—(*a*) SiO position-velocity diagram for I18264 along the axis denoted by the straight line in Fig. 3*a*. The gray scale and solid contours start at 2 σ in steps of 2 σ. The dashed contours mark the -2 σ level. (*b*) Same as (*a*), but for I23151 and along the axis denoted by the straight line in Fig. 5*a*. The contour levels start at 2.5 σ in steps of 2 σ, and the dashed contours represent the -2.5 σ level.

of the different pairs of SiO clumps and explain this in terms of multiple shocks driven by a processing and episodic jet. The downstream peak of the HC of the SE lobe in I18264 is farther away from the driving source than that of the VHC, which is similar to the SiO outflow in L1157, and the VHC of this outflow is offset north of the HC. We suggest that the SE lobe is driven by a precessing jet. In this scenario, the lower velocities of the HC than of the VHC imply a deceleration of the underlying jet after traveling a larger distance. The VHC is younger and driven by newly formed shocks when the underlying jet is precessing to the north, and its flattened mass spectrum and the very broad line width suggest it does not experience significant deceleration. In addition, the VHC of the northwest SiO clump is also slightly shifted to the south of the HC, and both the VHC and HC align with the VHC and HC of the SE lobe, respectively. This provides more evidence for the precessing scenario. Most recently, the VLA observations by Zapata et al. (2006) resolved the western millimeter peak in I18264 into triple sources at 1.3 cm and 7 mm. One of the three sources shows a slightly rising spectral index between 3.6 and 1.3 cm, and a flux density at 7 mm is larger than the value extrapolated from the 3.6 and 1.3 cm observations. Zapata et al. (2006) suggest that this source is a combination of a thermal jet and a disk. This is consistent with our interpretation that the SE lobe is being driven by a precessing jet.

In the case of I23151, the SiO outflow traces the inner parts of the large bipolar CO outflow despite the additional feature to the south. As described above, the blueshifted outflow is revealed as a quasi-parabolic structure, which is coincident with similar structures in the 3.4 mm continuum and $H^{13}CO^+$ line emission, as well as with the near-infrared conelike nebulosity by Weigelt et al. (2006). Apparently, this can be interpreted as the molecular outflow being entrained by a wide-angle wind, where the low-intensity SiO emission in the central region of the cone is due to the cavity cleared by the wind, while the enhanced SiO emission at the base of the outflow is caused by the interaction between the wind and the ambient material in the wall of the cavity. Weigelt et al. (2006) also reveal a bright point source at the tip of the conelike nebulosity. Since the point source is located at the center of the single-dish 1.2 mm peak, Weigelt et al. (2006) suggest that it is a protostar driving an outflow traced by the nebulosity. The astrometry of the point source is (R.A., decl.)(J2000.0) = ($23^h17^m21.02^s$, $59°28'48.0''$) from the comparison of the speckle image with the 2MASS images and 2MASS All-Sky Catalog of Point Sources. The position of the millimeter peak of our PdBI observations is (R.A., decl.)(J2000.0) = ($23^h17^m20.88^s$, $59°28'47.7''$). Considering the 2MASS positional accuracy of $1''$, the PdBI millimeter peak could be the same as the near-infrared point source. But it is also possible that the offset is real, that the very bright near-infrared point source is too evolved to be a protostar, and that the driving source of the outflow corresponds to the interferometric millimeter peak, which is not resolved in the single-dish 1.2 mm continuum with an $11''$ resolution.

The position-velocity (PV) diagrams of the SiO outflows along the axes marked in Figures 3*a* and 5*a* are shown in Figure 11. For I18264, in addition to the feature around the driving source with velocities near the systemic velocity, there are two main components in the PV diagram: the component with velocities increasing

linearly with the distance from the driving source and the component farther away from the driving source with maximum velocities decreasing with increasing distance. Compared with the channel maps in Figure 2, we find that these two components correspond to the VHC and HC of the SE lobe in Figure 3*b*. There is a pair of faint features centered at about $-27''$, which corresponds to the northwest lobe of the SE-NW outflow. The velocity structure of the peak emission of the VHC follows the so-called Hubble law and can be explained in terms of bow shock acceleration. This is compatible with the interpretation that the VHC is excited by the newly formed shocks without undergoing significant deceleration. If the broken power law results when the low-velocity ($|\Delta v| < 10$ km s^{-1}) gas comprises ambient gas entrained by the high-velocity ($|\Delta v| > 10$ km s^{-1}) gas (Su et al. 2004), the high-velocity gas should inject momentum into the low-velocity gas and decelerate when it travels downstream. This scenario is in agreement with the velocity structure of the HC in the PV diagram of I18264, where the maximum velocities decrease with distance from the driving source. For I23151, the PV diagram roughly follows the Hubble law. At the position about $7''$ from the driving source, emission features have a relatively wide range of velocities.

5. CONCLUSIONS

We carry out a study of SiO outflows toward the high-mass star-forming regions IRAS 18264−1152 and IRAS 23151+5912. According to the $H^{13}CO^+$ observations and SiO line profiles, the SiO emission in these two sources could be caused by the interaction between the jet or wind from the central young stars and the dense ambient gas. The mass-velocity relation of the HC of the SE lobe in I18264 and the blueshifted outflows in I23151 also can be fitted by a broken power law with the slopes steeping at about 10 km s^{-1} with respective to the systemic velocity. With the PV characteristic of the terminal velocities decreasing with distance from the driving source, the low-velocity ($|\Delta v| < 10$ km s^{-1}) gas probably comprises the ambient gas entrained by the high-velocity ($|\Delta v| > 10$ km s^{-1}) gas.

Toward I18264, at least two quasi-perpendicular outflows with high collimation factors (∼3–4) are resolved. The VHC of the SE lobe has very high velocities up to $\Delta v \sim 60$ km s^{-1}. It is offset north of the HC, and its downstream peak is farther away from the driving source. After comparing with the outflows in the well-studied low-mass source L1157, we suggest that the SE lobe could be entrained by an underlying precessing jet. The characteristics of the HC and VHC of the SE lobe in the mass-velocity and PV diagrams also support the processing jet scenario. For I23151, the blueshifted SiO emission traces a quasi-parabolic shaped outflow that can be identified in the 3.4 mm continuum and $H^{13}CO^+$ emission and coincides with the near-infrared nebulosity in the literature. This outflow can be interpreted as the molecular gas entrained by the underlying wide-angle wind.

The core masses estimated from the 3.4 mm continuum are 570 and 7300 $M_\odot$ for the near and far distances, respectively, for I18264 and 170 $M_\odot$ for I23151. With the assumption of momentum conservation between the outflow and the driving agent, the estimated outflow rates lead to accretion rates of 1.2×10^{-3} and 4.2×10^{-2} $M_\odot$ yr^{-1} for the near and far distances, respectively, for I18264 and 1.9×10^{-5} $M_\odot$ yr^{-1} for I23151. If we take into account the missing flux due to the missing short spacings for I23151, the accretion rate in this region would be higher. Thus, for both sources the accretion rates are high enough to overcome the radiation pressure from the central objects and form massive stars.

To summarize, our molecular outflow data derived from high-resolution observations toward two luminous sources show morphologies and kinematics similar to those of the low-mass sources. The outflows can be modeled as jets or wide-angle wind entrainment. The presented data and analysis further support the theory that massive stars up to 10^5 $L_\odot$ (∼30 $M_\odot$) form via disk-mediated accretion processes as do low-mass stars.

We are grateful to F. Geuth and the staff at PdBI for their help in the observations and data reduction. K. Q. acknowledges the support of grant 10128306 from NSFC. H. B. acknowledges financial support by the Emmy-Noether-Program of the Deutsche Forschungsgemeinschaft (DFG; grant BE2578).

REFERENCES

Bachiller, R., & Gutiérrez, M. P. 1997, ApJ, 487, L93
Bally, J., & Zinnecker, H. 2005, AJ, 129, 2281
Beuther, H., Schilke, P., & Gueth, F. 2004, ApJ, 608, 330
Beuther, H., Schilke, P., Gueth, F., McCaughrean, M., Andersen, M., Sridharan, T. K., & Menten, K. M. 2002a, A&A, 387, 931
Beuther, H., Schilke, P., Menten, K. M., Motte, F., Sridharan, T. K., & Wyrowski, F. 2002b, ApJ, 566, 945
Beuther, H., Schilke, P., Sridharan, T. K., Menten, K. M., Walmsley, C. M., & Wyrowski, F. 2002c, A&A, 383, 892
Beuther, H., Schilke, P., & Stanke, T. 2003, A&A, 408, 601
Beuther, H., Walsh, A., Schilke, P., Sridharan, T. K., Menten, K. M., & Wyrowski, F. 2002d, A&A, 390, 289
Bonnell, I. A., Bate, M. R., & Zinnecker, H. 1998, MNRAS, 298, 93
Bonnell, I. A., Vine, S. G., & Bate, M. R. 2004, MNRAS, 349, 735
Cesaroni, R., Felli, M., Jenness, T., Neri, R., Olmi, L., Robberto, M., Testi, L., & Walmsley, C. M. 1999, A&A, 345, 949
Chandler, C. J., Terebey, S., Barsony, M., Moore, T. J. T., & Gautier, T. N. 1996, ApJ, 471, 308
Danby, G., Flower, D. R., Valiron, P., Schilke, P., & Walmsley, C. M. 1988, MNRAS, 235, 229
Downes, T. P., & Ray, T. P. 1999, A&A, 345, 977
Garay, G., & Lizano, S. 1999, PASP, 111, 1049
Gibb, A. G., Hoare, M. G., Little, L. T., & Wright, M. C. H. 2003, MNRAS, 339, 1011
Girart, J. M., Viti, S., Estalella, R., & Williams, D. A. 2005, A&A, 439, 601
Guilloteau, S., Bachiller, R., Fuente, A., & Lucas, R. 1992, A&A, 265, L49
Hildebrand, R. H. 1983, QJRAS, 24, 267
Hirano, N., Mikami, H., Umemoto, T., Yamamoto, S., & Taniguichi, Y. 2001, ApJ, 547, 899
Ho, P. T. P., & Townes, C. H. 1983, ARA&A, 21, 239
Hunter, T. R., Testi, L., Zhang, Q., & Sridharan, T. K. 1999, AJ, 118, 477
Jijina, J., & Adams, F. C. 1996, ApJ, 462, 874
Jørgensen, J. K., Hogerheijde, M. R., Blake, G. A., van Dishoeck, E. F., Mundy, L. G., & Schöier, F. L. 2004, A&A, 415, 1021
Keto, E. 2003, ApJ, 599, 1196
Krumholz, M. R., McKee, C. F., & Klein, R. I. 2005a, Nature, 438, 332
———. 2005b, ApJ, 618, L33
Kumar, M. S. N., Tafalla, M., & Bachiller, R. 2004, A&A, 426, 195
Lada, C. J., & Fich, M. 1996, ApJ, 459, 638
Langer, W., & Penzias, A. 1990, ApJ, 357, 477
McKee, C. F., & Tan, J. C. 2002, Nature, 416, 59
———. 2003, ApJ, 585, 850
Mikami, H., Tomofumi, U., Yamamoto, S., & Saito, S. 1992, ApJ, 392, L87
Norberg, P., & Maeder, A. 2000, A&A, 359, 1025
Quillen, A. C., Thorndike, S. L., Cunningham, A., Frank, A., Gutermuth, R. A., Blackman, E. G., & Pipher, J. L. 2005, ApJ, 632, 941
Richer, J., Shepherd, D., Cabrit, S., Bachiller, R., & Churchwell, E. 2000, in Protostars and Planets IV, ed. V. Mannings, A. Boss, & S. Russell (Tucson: Univ. Arizona Press), 867
Ridge, N. A., & Moore, T. J. T. 2001, A&A, 378, 495
Schike, P., Walmsley, C. M., Pineau des Forêts, G., & Flower, D. R. 1997, A&A, 321, 293

Seab, C. G., & Shull, J. M. 1983, ApJ, 275, 652
Sewilo, M., Watson, C., Araya, E., Churchwell, E., Hofner, P., & Kurtz, S. 2004, ApJS, 154, 553
Shepherd, D. S., & Churchwell, E. 1996, ApJ, 472, 225
Shepherd, D. S., & Kurtz, S. E. 1999, ApJ, 523, 690
Shepherd, D. S., Testi, L., & Stark, D. P. 2003, ApJ, 584, 882
Shepherd, D. S., Yu, K. C., Bally, J., & Testi, L. 2000, ApJ, 535, 833
Shu, F. H., Adams, F. C., & Lizano, S. 1987, ARA&A, 25, 23
Smith, M. D., Suttner, G., & Yorke, H. W. 1997, A&A, 323, 223
Sollins, P. K., et al. 2004, ApJ, 616, L35
Sridharan, T. K., Beuther, H., Schilke, P., Menten, K. M., & Wyrowski, F. 2002, ApJ, 566, 931
Stahler, S. W., Palla, F., & Ho, P. T. P. 2000, in Protostars and Planets IV, ed. V. Mannings, A. Boss, & S. Russell (Tucson: Univ. Arizona Press), 867
Su, Y.-N., Zhang, Q., & Lim, J. 2004, ApJ, 604, 258
Tomisaka, K. 1998, ApJ, 502, L163
van Dishoeck, E. F., Blake, G. A., Draine, B. T., & Lunine, J. I. 1993, in Protostars and Planets III, ed. E. H. Levy & J. I. Lunine (Tucson: Univ. Arizona Press), 163
Walmsley, C. M., & Ungerechts, H. 1983, A&A, 122, 164
Weigelt, G., Beuther, H., Hofmann, K.-H., Meyer, M. R., Preibisch, Th., Schertl, D., Smith, M. D., & Young, E. T. 2006, A&A, 447, 655
Wolfire, M. G., & Cassinelli, J. P. 1987, ApJ, 319, 850
Yorke, H. W., & Sonnhalter, C. 2002, ApJ, 569, 846
Zapata, L. A., Rodriguez, L. F., Ho, P. T. P., Beuther, H., & Zhang, Q. 2006, AJ, 131, 939
Zhang, Q., Ho, P. T. P., & Wright, M. C. H. 2000, AJ, 119, 1345
Zhang, Q., Ho, P. T. P., Wright, M. C. H., & Wilner, D. J. 1995, ApJ, 451, L71
Zhang, Q., Hunter, T. R., Brand, J., Sridharan, T. K., Cesaroni, R., Molinari, S., Wang, J., & Kramer, M. 2005, ApJ, 625, 864
Zhang, Q., Hunter, T. R., Brand, J., Sridharan, T. K., Molinari, S., Kramer, M. A., & Cesaroni, R. 2001, ApJ, 552, L167
Ziurys, L. M., Friberg, P., & Irvine, W. M. 1989, ApJ, 343, 201